Journal of Manufacturing Processes 161 (2026) 34–48

Contents lists available at ScienceDirect

Journal of Manufacturing Processes

journal homepage: www.elsevier.com/locate/manpro

Experimental investigation and numerical validation of drilling machinability in FDM-printed PLA parts

Uğur Köklü [a,b], Levent Urtekin [c], Erkin Akdoğan [a], Faik Yılan [c], Murat Demiral [d,*]

[a] Karamanoğlu Mehmetbey University, Department of Mechanical Engineering, Karaman, Turkey
[b] Department of Mechanical Engineering, Recep Tayyip Erdogan University, Rize, Turkey
[c] Kırşehir Ahi Evran University, Department of Mechanical Engineering, Kırşehir, Turkey
[d] College of Engineering and Technology, American University of the Middle East, Egaila 54200, Kuwait

HIGHLIGHTS

- Infill density strongly governs tensile strength, stiffness, and hardness.
- Grid infill at 215 °C, 100% density gave peak strength and stiffness.
- Hexagonal infill improved strength-to-weight and drilling performance.
- Higher print temps (200–215 °C) enhanced bonding and reduced voids.
- Low feed, high speed drilling minimized delamination and hole damage.

ARTICLE INFO

Keywords:
Additive manufacturing
Fused deposition modeling
PLA
Infill pattern
Tensile strength
Drilling
Thrust force
Surface quality
Machinability

ABSTRACT

Fused Deposition Modeling (FDM) is a widely used additive manufacturing technique that fabricates components through layer-by-layer deposition of thermoplastic materials. Due to its biodegradability, dimensional stability, and favorable flow behavior, polylactic acid (PLA) has become one of the most commonly employed polymers in extrusion-based printing. This study investigates the influence of extrusion temperature, infill pattern, and infill density on the mechanical performance and drilling machinability of FDM-printed PLA components. Tensile tests and hardness measurements were conducted to evaluate mechanical behavior, while drilling machinability was assessed through thrust force measurements and digital microscopy. In parallel, a three-dimensional finite element model was developed using ABAQUS/Explicit to capture damage initiation and interfacial degradation, providing numerical validation of the experimental results. The findings demonstrate that infill density is the dominant parameter, with higher densities leading to significant improvements in tensile strength, elastic modulus, and surface hardness. The grid infill at full density and elevated extrusion temperature yielded the highest mechanical performance, achieving a tensile strength of 40.3 MPa and a modulus of 3050 MPa. In contrast, the hexagonal infill pattern offered a favorable balance between mechanical strength and drilling performance, exhibiting reduced thrust force and improved damage resistance. Optimal drilling conditions were identified at 3000 rpm and 150 mm/min, minimizing delamination, burr formation, and thermal damage. Overall, this work highlights the strong coupling between process parameters, internal architecture, and numerical modeling in governing the structural integrity and machinability of FDM-fabricated PLA parts.

1. Introduction

Additive Manufacturing (AM), commonly known as 3D printing and previously referred to as rapid prototyping, is the formal term for technologies that create objects by adding material layer by layer [1–4]. The working principle of additive manufacturing; it is based on the logic of creating the final product by adding material layer by layer and differs from traditional manufacturing methods such as welding, joining, milling, soldering, casting, brazing, CNC turning processes, extrusion, powder metallurgy, and cutting [5–7]. In AM applications, production is

* Corresponding author.
E-mail address: murat.demiral@aum.edu.kw (M. Demiral).

https://doi.org/10.1016/j.jmapro.2026.01.079
Received 7 October 2025; Received in revised form 17 January 2026; Accepted 24 January 2026
Available online 31 January 2026

carried out almost without limitation in the geometry of a structure, using all types of materials (polymers, metals and ceramics). Therefore, the additive manufacturing method continues to progress in the automotive, aerospace, healthcare, food, construction, energy and other industries due to its unique features [8].

Fused Deposition Modeling (FDM) is a widely used additive manufacturing technique [9,10] in which a thermoplastic filament is heated to a semi-molten state and extruded through a nozzle, then deposited sequentially in a layer-by-layer manner onto a build platform. Each deposited layer partially remelts and thermally bonds with the underlying layer before solidifying upon cooling, progressively forming the intended three-dimensional structure [11–14]. However, the layer-wise deposition process inherently introduces microstructural discontinuities, such as interlayer weak bonding, void formation, and the stair-stepping effect at layer interfaces. These features lead to anisotropic mechanical behavior, reduced interlaminar strength, and surface irregularities, which can significantly influence load transfer, damage initiation, and chip formation during machining operations. Consequently, the mechanical performance and drilling machinability of FDM-fabricated parts are strongly dependent on process parameters and internal architecture, necessitating systematic investigation and validation.

In the scientific literature, most studies in this field have concentrated on examining the influence of process parameters on the mechanical properties of PLA samples [15–17]. For example, Gonabadi et al. [18] investigated the effects of build orientation and infill density on the mechanical behavior of PLA specimens and reported that tensile strength was not significantly affected by changes in infill pattern. Similarly, Yılan et al. [19] studied the influence of infill pattern, infill density, and print speed on the tensile strength and production time of PLA models. Their results indicated that a triangle infill pattern provided the highest tensile strength at a printing speed of 40 mm/s and 100% infill density. Furthermore, Valean et al. [20] analyzed the effects of seven process parameters—infill pattern, infill density, printing orientation, layer thickness, printing speed, nozzle temperature, and number of outer layers—on the tensile behavior of printed dog-bone specimens produced by the MEX process. The optimal combination of parameters was identified as TR-IP, 100%-ID, 0°-PO, 0.2 mm-LT, 20 mm/s-PS, 220°C-NT, and 3-NOL, yielding a maximum tensile strength of 62.42 MPa, a fracture energy of 1.46 MJ/m^3, and high dimensional accuracy. These optimized results exceeded most reported tensile strengths for MEX-printed and even injection-molded PLA parts. Nonetheless, significant uncertainties still persist regarding the influence of specific process parameters [21].

In recent years, FDM systems have been widely preferred because of their cheapness, simplicity, easy filaments supply and producing high quality products in a short time. In addition, PLA filaments based on thermoplastic polymers are used in FDM [22–24]. This can be attributed to its many positive features of PLA such as non-toxic, low cost, tough, environmentally friendly and strong [25]. In spite of this beneficial influence, as with other production methods, the FDM method has its disadvantages [26]. Because, as well-known, polymer parts printed with FDM exhibit poor surface properties. This indicates that the precision of polymer parts must be guaranteed in aerospace structures. Hence, there is a usually needed for machining operations processing of the final samples [27]. Batista et al. [28] presented the first approach to the feasibility of drilling parts obtained with FDM. They examined how PETG material selection and processing with different layer thicknesses can affect its geometric properties. Dezaki et al. [29] obtained the best surface quality for 20 mm holes in printed PLA samples at a feed rate of 1100 mm/min and a spindle speed in the range of 800–1000 rpm to examine the effects of structure orientation. Kumar and Jayakumar [30] optimized the mechanical characterization, average surface roughness (R_a) and delamination (F_d) of particle reinforced PLA samples. In their study, they emphasized that the diameter of the drill bit, spindle and feed rate affect both R_a and F_d. Ulkir [31] demonstrated the complex interactions between FDM parameters—layer thickness, infill density, and nozzle temperature—and the mechanical and thermal behavior of metal-reinforced PLA composites, highlighting challenges in multi-objective optimization of printing performance [32]. Baraheni et al. [33] showed that ultrasonic drilling improves the mechanical quality of FDM-printed PLA parts by reducing thrust force, delamination, surface roughness, and geometrical deviations, with 4-flute end mills performing better than 2-flute. Multi-response optimization using ANOVA and NSGA-II highlights the significant factors affecting mechanical performance.

A review of the literature shows that the drilling performance of FDM-printed parts has been scarcely studied [34]. In particular, no studies have systematically examined PLA materials while considering infill density, geometric pattern, and printing speed as key FDM process parameters. To address this gap, the present study investigates the combined effects of extrusion temperature, infill pattern, and infill density on the tensile strength, hardness, and drilling machinability (thrust force and hole quality) of FDM-printed PLA. A major novelty is the development and validation of a 3D finite element model that incorporates both intra-layer damage (via Hashin criteria) and inter-layer delamination (via cohesive surfaces) to simulate the drilling process, providing insight into the underlying failure mechanisms. The study combines this numerical approach with experiments—including tensile testing, Shore-D hardness measurements, drilling thrust force, and hole surface characterization via digital microscopy—offering a comprehensive understanding of how internal design parameters influence both the structural integrity and post-processing behavior of biodegradable thermoplastic parts produced by additive manufacturing.

2. Materials and methods

2.1. Sample preparation

In this study, specimens have been fabricated using a 3D FDM device that was designed and manufactured in-house [19]. Table 1 shows the mechanical properties of PLA. Notably, it is considered to analyze PLA filament material that used to be commonly implemented in 3D printings. Namely, PLA (eSUN:3d-∅1.75 mm) specimens.

The printing parameters were optimized through preliminary trials to ensure continuous material flow, dimensional accuracy, and the absence of surface defects. During fabrication, both variable and fixed parameters were carefully controlled to ensure reproducibility by minimizing the influence of environmental or machine-related variations. The fixed parameters included the nozzle diameter, bed temperature, printing speed, layer height, and the number of solid layers, which were kept identical for all specimens throughout the entire printing process. These values were determined according to standard PLA printing guidelines and preliminary tests to ensure stable extrusion and consistent deposition quality. The complete set of fixed parameters are summarized, in Table 2.

In this study, specimens were fabricated using varying extrusion temperatures, infill patterns, and infill percentages, as detailed in Table 3. The samples were produced at three different extrusion temperatures (185 °C, 200 °C, and 215 °C), three distinct infill patterns (Grid, Hexagonal, and Concentric), and five different infill percentages (20%, 40%, 80%, and 100%). Each specimen was manufactured according to the specified parameter combinations to investigate the effects of these variables on mechanical properties. Standard

Table 1
Materials properties of PLA [35,36].

Density (g/cm^3)	Tensile strength (MPa)	Poisson ratio	Young's modulus (GPa)	Bulk modulus (GPa)	Shear modulus (GPa)
1.23	63	0.3	2.3	1.91	8.84

Table 2
Fixed 3D printing parameters used in the fabrication of PLA specimens.

Parameter (units)	Value
Nozzle size (mm)	0.6
Bed temperature (°C)	42
Printing speed (mm/s)	100
Layer height (mm)	0.2
Top solid layers	4
Bottom solid layers	4
Extruder quantity	single
Cooling fan speed (mm/s)	100
Positioning accuracy (mm)	X/Y: 0.012, Z: 0.002
Printing environment (°C)	25 ± 2 ambient
Build volume (mm^3)	220 × 220 × 250
Firmware	Marlin
Slicing software	Ultimaker Cura
Outer wall speed (mm/s)	Same as printing speed (kept constant)
Number of outer shells	2

Table 3
Manufacturing parameters for 3D-printed specimens: extrusion temperature, infill pattern, and infill percentage variations.

Specimen	Extrusion temperature, (°C)	Infill patterns	Infill percentage %
200_Grid_20	200	Grid	20
200_Grid_40	200	Grid	40
215_Grid_40	215	Grid	40
185_Grid_80	185	Grid	80
200_Grid_80	200	Grid	80
200_Grid_100	200	Grid	100
215_Grid_100	215	Grid	100
200_Hex_20	200	Hexagonal	20
215_Hex_20	215	Hexagonal	20
185_Hex_40	185	Hexagonal	40
200_Hex_40	200	Hexagonal	40
200_Hex_80	200	Hexagonal	80
200_Hex_100	200	Hexagonal	100
185_Conc_20	185	Concentric	20
200_Conc_20	200	Concentric	20
200_Conc_40	200	Concentric	40
200_Conc_80	200	Concentric	80
215_Conc_80	215	Concentric	80
185_Conc_100	185	Concentric	100
200_Conc_100	200	Concentric	100

manufacturing conditions were maintained throughout the production process to ensure consistency across all parameter sets. This comprehensive variation of parameters allowed for a detailed analysis of material performance. The selection of extrusion temperature, infill pattern, and infill density levels was guided by a controlled experimental design strategy aimed at capturing representative processing conditions while avoiding unstable or non-reproducible regimes. The extrusion temperature range of 185–215 °C was defined based on commonly reported processing windows for PLA in FDM applications, where lower temperatures favor dimensional stability and higher temperatures enhance polymer chain mobility and interlayer bonding, as generally discussed in the literature [31,32,37].

The infill patterns selected in this study (Grid, Hexagonal, and Concentric) are among the most widely adopted internal geometries in FDM research and are known to exhibit distinct load transfer paths and structural continuity, making them suitable for systematic structure–property evaluations [19]. Similarly, infill density levels ranging from 20% to 100% were chosen to represent a gradual transition from highly porous to fully dense internal structures, allowing the isolated and combined effects of material distribution on mechanical performance and drilling machinability to be assessed, consistent with established experimental methodologies reported in earlier works [19]. Preliminary printing trials confirmed that all selected parameter combinations provided stable extrusion conditions and defect-free specimen fabrication.

2.2. Tests and characterization

Prior to testing, all specimens were conditioned for 40 h at 50% relative humidity and 23 °C, following the ASTM D618 standard. The tensile tests of the 3D-printed PLA specimens were then performed in accordance with the ASTM D638 standard, using Type IV specimen geometry, which specifies the procedure for evaluating the tensile properties of plastics [35]. The tests were conducted using a Shimadzu AGS-X universal testing machine (Fig. 1(a)) equipped with a 100 kN load cell, operating at a constant crosshead speed of 5 mm/min. For each specimen type, three samples were tested to ensure repeatability. The tensile strength and elastic modulus were calculated from the stress–-strain curves obtained during testing.

Additionally, hardness measurements were carried out using an X.F Shore D hardness tester (Fig. 1(b)), in compliance with the ASTM D2240 standard. These tests provided complementary data on the surface resistance and mechanical integrity of the printed PLA specimens.

All machining experiments were performed on a Quaser MV154C vertical machining center, equipped with a high-speed spindle capable of reaching 10,000 rpm and delivering a maximum power output of 17.5 kW, providing stable and consistent cutting conditions during testing (Fig. 2(a)). The workpiece material consisted of flat PLA plates with dimensions of 200 mm × 200 mm × 5 mm (length × width × thickness).

All experiments were conducted under dry machining conditions (without cutting fluid), focusing solely on drilling operations. Drilling was carried out at spindle speeds of 1500 rpm and 3000 rpm, with corresponding feed rates of 150 mm/min and 300 mm/min, respectively. For each cutting condition, three holes were drilled on each specimen to ensure repeatability and reliability of the results.

A 6 mm solid carbide twist drill, coated with Titanium Silicon Nitride (TiSiN) and featuring a tungsten carbide substrate, was used for all tests. The thrust force generated during drilling was recorded in real-time using a Kistler 9257B piezoelectric dynamometer connected to a 5070 amplifier (Fig. 2(b)) and a 5697 A data acquisition system (Fig. 2(c)) [38,39].

During PLA drilling operations, monitoring of cutting forces indicated that the thrust force (Fz) accounted for virtually all machining forces, while planar components (Fx, Fy) were insignificant. A standard twist drill bit with a diameter of 6 mm was used for all drilling operations (Fig. 3). The resulting hole quality was quantitatively assessed through microscopic examination of exit surfaces using a Keyence VHX 900 digital microscope (Fig. 4).

2.3. Numerical modeling

This section describes the numerical framework adopted to simulate the drilling of PLA components produced via FDM. A 3D finite element

Fig. 1. (a) Shimadzu AGS-X universal testing machine and (b) X.F Shore D hardness tester.

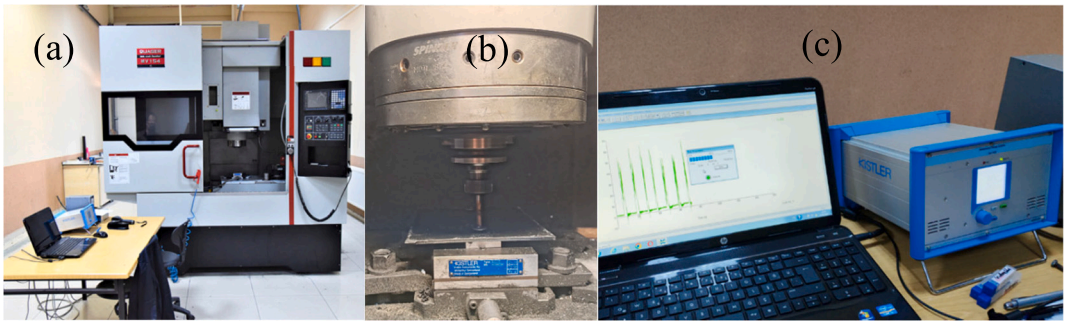

Fig. 2. (a) Quaser MV154C vertical machining center, (b) piezoelectric dynamometer coupled with a 5070 amplifier and (c) 5697 A data acquisition system.

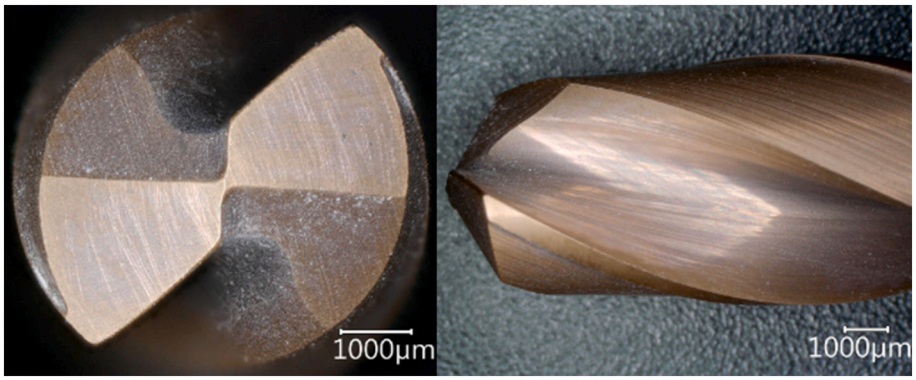

Fig. 3. A standard twist drill bit with a diameter of 6 mm.

Fig. 4. Keyence VHX 900 digital microscope.

(FE) model was developed in ABAQUS/Explicit to provide additional insight into deformation and damage mechanisms observed during experiments (see Fig. 5). The model geometry represented a rectangular PLA plate (80 mm × 80 mm × 5 mm), discretized primarily with 8-node continuum shell elements (SC8R). To capture localized stress concentrations and failure near the tool–workpiece interaction zone, a refined mesh of 0.25 mm was employed around the drilling region, while a coarser mesh was applied elsewhere to reduce computational cost. The 6 mm drill bit was modeled as a rigid body meshed with R3D4 elements, constrained to translate along the negative y-axis and rotate about its axis at speeds between 1500 and 3000 rpm, replicating experimental drilling conditions. Hourglass control and distortion stabilization were applied to suppress non-physical deformations.

To simulate the interaction between the drill bit and the PLA workpiece, the General Contact Algorithm in ABAQUS/Explicit was employed. Normal contact was enforced through a kinematic constraint approach, while tangential behavior followed a Coulomb friction law with a coefficient of $\mu = 0.4$ [40]. All external boundaries of the PLA plate were fixed to prevent rigid-body motion, with local release at the drilling zone to replicate realistic boundary conditions.

Material failure was modeled using a continuum damage mechanics framework to capture intra-layer deformation and fracture, while interlayer separation between printed filaments (0.2 mm each) was represented through cohesive surface elements. Detailed descriptions of these damage modeling approaches are presented in the following.

Intra-layer failure within the PLA specimens was modeled using a continuum damage mechanics (CDM) framework combined with an orthotropic constitutive law. Damage initiation was described using a three-dimensional failure criterion adapted from Hashin's model [41], allowing the prediction of failure under different loading conditions.

Material degradation was assumed to begin once the equivalent stress exceeded a critical threshold, after which progressive stiffness reduction was applied. Four failure mechanisms were considered: filament-direction tension (*ft*), filament-direction compression (*fc*),

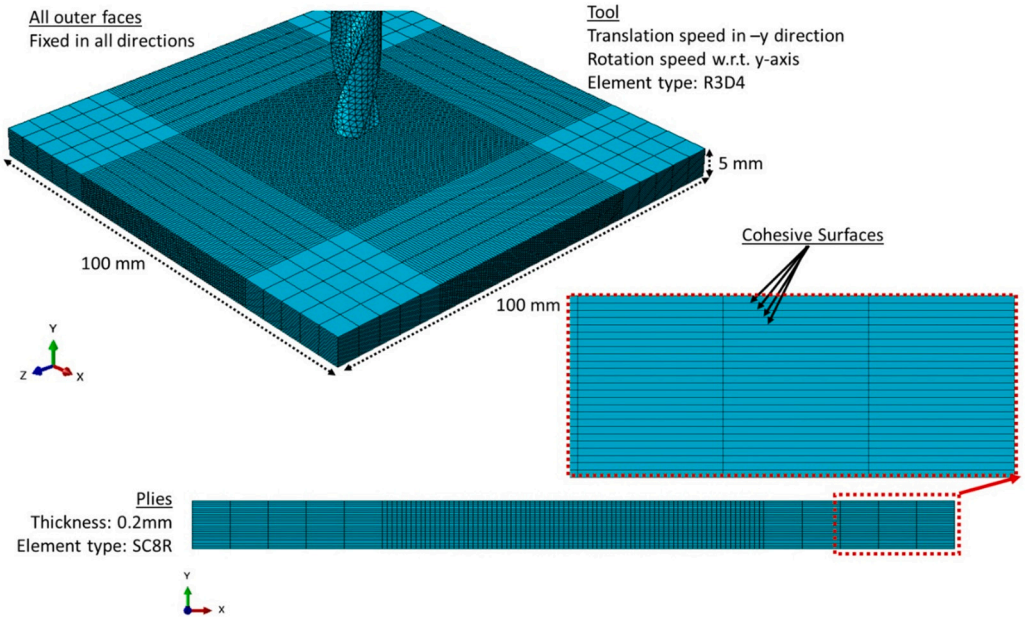

Fig. 5. Three-dimensional ABAQUS/Explicit finite-element model for drilling of FDM-fabricated PLA.

transverse (interlayer) tension (*mt*), and transverse compression (*mc*). The corresponding failure indicators (Table 4) were formulated in terms of the stress components σ_{ij}, with failure in a particular mode occurring once the indicator reached unity. Here, X^T and X^C denote tensile and compressive strengths along the filament direction, while Y^T and Y^C represent tensile and compressive strengths transverse to the deposition path (interlayer direction). Shear strengths were defined as S^L (longitudinal) and S^T(transverse). A shear interaction parameter of $\alpha = 1.0$ was adopted. PLA was assumed to behave elastically until the onset of one of the failure criteria.

When damage evolution was activated, the effective stress in the material was scaled by the corresponding damage variable, reducing the load-carrying capacity of the PLA filaments and interlayer regions. The stiffness degradation was applied independently for each failure mode, with the total response obtained by superimposing the contributions of filament-direction and interlayer failures. Complete material failure was assumed once the damage variable reached unity, at which point the element was considered fully degraded and removed from the simulation. The related equations and description of the terms used are presented in Table 4. Additional details of the model can be found in [42].

The stresses in a damaged element are determined through the classical stress–strain relation, $\sigma = C_d\varepsilon$, where the degraded stiffness matrix C_d reflects the reduction in stiffness that develops during the damage progression of the plies, expressed as:

$$C_d = \frac{\begin{bmatrix} E_{11}(1-d_f) & E_{11}\vartheta_{21}(1-d_f)(1-d_m) & 0 \\ E_{22}\vartheta_{12}(1-d_f)(1-d_m) & E_{22}(1-d_m) & 0 \\ 0 & 0 & G_{12}D(1-d_s) \end{bmatrix}}{D}$$

$$D = 1-(1-d_f)(1-d_m)\vartheta_{12}\vartheta_{21}$$

$$d_f = \begin{cases} d_f^T & \text{if } \sigma_{11} \geq 0 \\ d_f^C & \text{if } \sigma_{11} < 0 \end{cases}$$

$$d_m = \begin{cases} d_m^T & \text{if } \sigma_{22} \geq 0 \\ d_m^C & \text{if } \sigma_{22} < 0 \end{cases}$$

$$d_s = 1-(1-d_f)^*(1-d_m) \quad (1)$$

where, E_{ij}, ϑ_{ij}, G_{ij} represent the engineering constants of the material, while d_f, d_m and d_s correspond to the damage variables representing the current states of filament-direction, interlayer, and shear damage, respectively. The elastic, strength, and damage parameters implemented in Abaqus for the PLA simulations are summarized in Table 5.

The maximum in-plane characteristic length of an undeformed continuum element—calculated as the square root of the product of its in-plane dimensions—was constrained to remain smaller than the critical length required to prevent snap-back in the constitutive softening response, given by $2G_IE_I/\sigma_I$ [43], where I = filament tension (*ft*), filament compression (*fc*), interlayer tension (*mt*), and interlayer compression (*mc*). This criterion guided the selection of element size for modeling the PLA domains. During the simulations, an element was

Table 4
Details of 3D failure criteria.

	Failure mode	Condition	Constitutive equations
Damage initiation	*ft*	$\sigma_{11} \geq 0$	$f_1 = \left(\frac{\sigma_{11}}{X^T}\right)^2 + \alpha\left(\frac{\sigma_{12}}{S^L}\right)^2$
	fc	$\sigma_{11} < 0$	$f_2 = \left(\frac{\sigma_{11}}{X^C}\right)^2$
	mt	$\sigma_{22} \geq 0$	$f_3 = \left(\frac{\sigma_{22}}{Y^T}\right)^2 + \left(\frac{\sigma_{12}}{S^L}\right)^2$
	mc	$\sigma_{22} < 0$	$f_4 = \left(\frac{\sigma_{22}}{2S^T}\right)^2 + \left[\left(\frac{Y^C}{2S^T}\right)^2 - 1\right]\frac{\sigma_{22}}{Y^C} + \left(\frac{\sigma_{12}}{S^L}\right)^2$
Damage evolution	*ft, fc, mt, mc*		$d_I = \frac{\delta_{I,eq}^f\left(\delta_{I,eq} - \delta_{I,eq}^0\right)}{\delta_{I,eq}\left(\delta_{I,eq}^f - \delta_{I,eq}^0\right)}$ $\delta_{I,eq}^0$: the equivalent displacements at the initiation of damage for the respective mode $\delta_{I,eq}^f = 2G_I/\sigma_{I,eq}$: the equivalent displacements at the completion of damage for the respective mode G_I: the fracture toughness of the respective mode $\sigma_{I,eq}$: the equivalent stress of the respective mode $\delta_{I,eq}$: the equivalent displacement of the respective mode

Table 5
Material properties of PLA used in the numerical analyses [44].

Elastic (MPa)				
$E_{11} = E_{22}$	$\vartheta_{12}, \vartheta_{13}, \vartheta_{23}$	G_{12}	G_{13}	G_{23}
2890	0.35	817	817	817

Strength (MPa)					
X^T	X^C	Y^T	Y^C	S^L	S^T
39	39	39	39	8.4	8.4

Damage (N/mm)			
G_{ft}	G_{fc}	G_{mt}	G_{mc}
18	18	2	2

deleted from the mesh once the stiffness at all integration points had fully degraded, indicating complete material failure.

Cohesive surfaces were introduced at the interfaces of the composite layers to capture their traction–separation behavior. Delamination along these interfaces was evaluated using a parameter that quantified the degree of damage. In the finite element model, the quadratic nominal stress criterion was applied, indicating that interfacial damage initiates once the normalized stress reaches unity [45]. For cohesive surfaces, this criterion is expressed as:

$$\begin{aligned} &\textit{Damage initiation} \quad \left(\frac{\langle t_1 \rangle}{t_1^0}\right)^2 + \left(\frac{\langle t_2 \rangle}{t_2^0}\right)^2 + \left(\frac{\langle t_3 \rangle}{t_3^0}\right)^2 = 1 \\ &\text{Damage evolution} \quad \left(\frac{G_1}{G_1^0}\right)^\eta + \left(\frac{G_2}{G_2^0}\right)^\eta + \left(\frac{G_3}{G_3^0}\right)^\eta = 1 \end{aligned} \tag{2}$$

In this formulation, t_i, $i = 1, 2, 3$ denote the normal and the first and second shear traction components at the cohesive surface, while t_i^0 represent the corresponding interfacial strengths that define the onset of separation for each failure mode: Mode I (normal), Mode II (first shear), and Mode III (second shear).

The evolution of damage, governed by fracture energy, was modeled using a mixed-mode damage approach that applies a power-law fracture criterion to capture the interaction of different loading modes (see Eq. 2). In this relation, G_i corresponds to the instantaneous fracture energy for each failure mode, whereas G_i^0 represents the critical fracture energy required to initiate failure in Modes I, II, and III, respectively. The parameter η characterizes the material's sensitivity to mode mixity, which was taken as 2.0 in this study.

The traction–separation response of the cohesive interface exhibits a linear elastic behavior in the normal and two shear directions, represented by stiffness coefficients K_{11}, K_{22}, and K_{33}. This linear regime continues until the maximum traction, t_i^0, is reached, signifying the initiation of separation. Beyond this point, damage evolves and the stiffness progressively degrades. The extent of damage is quantified by the scalar variable ***CSDMG*** [46], ranging from 0 (undamaged) to 1 (completely damaged), and is expressed as:

$$CSDMG = \frac{\delta_m^f \left(\delta_m^{max} - \delta_m^0\right)}{\delta_m^{max}\left(\delta_m^f - \delta_m^0\right)} \tag{3}$$

In this formulation, δ_m^{max} represents the maximum effective displacement attained during the process, whereas δ_m^f and δ_m^0 correspond to the effective displacements at complete failure and at damage initiation, respectively. The cohesive constants used in the finite element model are listed in Table 6. In the simulations, the delamination factor (*DF*) was determined as the ratio of the delaminated area (*DA*) to the nominal hole area (*NA*), expressed as $DF = DA / NA$.

Table 6
Interface properties of PLA interlayer surfaces used in the numerical analyses [47].

K_{11} (MPa/mm)	K_{22}, K_{33} (MPa/mm)	t_1^0 (MPa)	$t_2^0 = t_3^0$ (MPa)	G_1^0 (N/mm)	G_2^0, G_3^0 (N/mm)
1×10^3	5×10^1	2	26	0.39	0.42

3. Results and discussion

3.1. Tensile properties and hardness

The experimental findings related to the tensile strength and hardness of PLA specimens produced under various FDM printing conditions are presented and analyzed. Emphasis was placed on evaluating the effects of printing temperature, infill pattern, and infill density on mechanical behavior. The results are illustrated through comparative bar charts, allowing for the identification of performance trends and notable differences between process settings. These insights contribute to a better understanding of how to optimize additive manufacturing parameters for enhanced material strength.

The experimental results summarizing the tensile strength, elastic modulus, and Shore-D hardness values of PLA specimens fabricated under different process parameters are presented in Table 7. As observed in the data, both the infill density and infill pattern significantly influenced the mechanical behavior of the printed parts. For instance, tensile strength values increased steadily with higher infill percentages across all patterns, with the highest value of 40.5 MPa obtained in the 215_Grid_100 condition. Similarly, specimens with concentric and hexagonal patterns demonstrated high strength at elevated infill densities, reaching up to 38.6 MPa and 39.3 MPa, respectively. The data in Table 7 also reveal a direct relationship between infill density and elastic modulus, as well as a general trend of increasing surface hardness with increased density.

The tensile strength values of PLA specimens were highly dependent on both the infill pattern and the printing parameters, as shown in Fig. 6 (1). For the grid pattern (Fig. 6 (1a)), the highest tensile strength was measured as 40.5 MPa at 215 °C and 100% infill, indicating a strong interlayer bonding and homogeneous stress distribution. The improvement of mechanical strength with increasing infill density is consistent with previous findings, which reported a positive correlation between density and strength in plan PLA-FDM prints [48,49].

The hexagonal pattern (Fig. 6 (1b)) exhibited a peak tensile strength

Table 7
Tensile test and hardness test results of 3D printed specimens.

Specimen	Tensile strength (MPa)	Modulus of elasticity (MPa)	Hardness (shore-D)
200_Grid_20	22.3 ± 0.2	1733 ± 9	64.3 ± 3
200_Grid_40	25.1 ± 0.2	1940 ± 8	72.7 ± 2
215_Grid_40	24 ± 0.2	1870 ± 27	74 ± 2
185_Grid_80	29.4 ± 0.4	2432 ± 24	78 ± 2
200_Grid_80	28.8 ± 0.4	2189 ± 12	81.1 ± 1
200_Grid_100	35.5 ± 0.5	2722 ± 45	81.7 ± 1
215_Grid_100	40.5 ± 0.4	3045 ± 37	81.9 ± 2
200_Hex_20	25.4 ± 0.4	1856 ± 22	74 ± 2
215_Hex_20	23.1 ± 0.3	1766 ± 17	67.3 ± 3
185_Hex_40	25.5 ± 0.3	2001 ± 41	73.4 ± 2
200_Hex_40	25.3 ± 0.6	1962 ± 43	77.1 ± 1
200_Hex_80	39.3 ± 0.4	2928 ± 50	80.3 ± 3
200_Hex_100	39.3 ± 0.4	2964 ± 41	78.3 ± 3
185_Conc_20	27 ± 0.2	1957 ± 32	65.9 ± 3
200_Conc_20	24.1 ± 0.4	1870 ± 32	74.7 ± 2
200_Conc_40	31.9 ± 0.3	2293 ± 34	73.3 ± 2
200_Conc_80	35.4 ± 0.4	2575 ± 25	81.4 ± 2
215_Conc_80	28.5 ± 0.4	2256 ± 35	76.3 ± 2
185_Conc_100	38.6 ± 0.4	3013 ± 27	78.9 ± 3
200_Conc_100	35 ± 0.3	2775 ± 28	82.7 ± 2

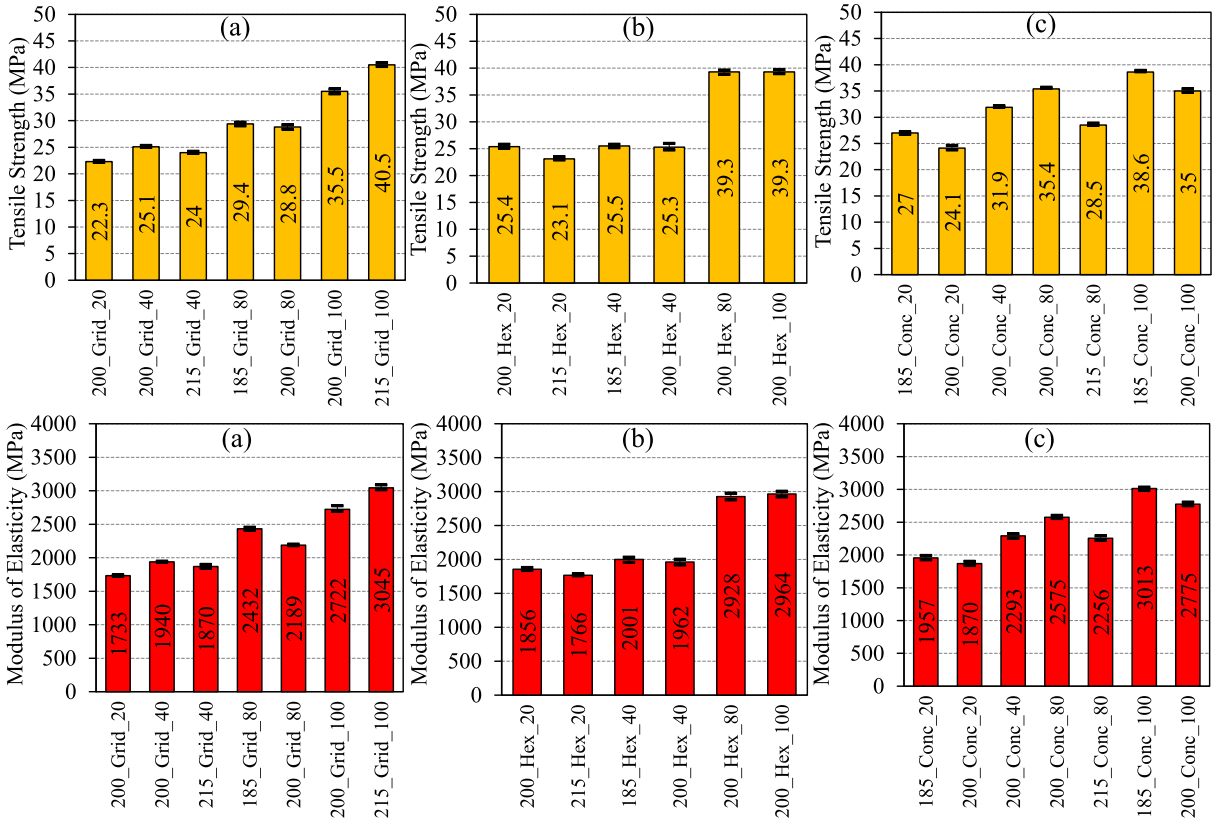

Fig. 6. Tensile strength (1) and modulus of elasticity (2) test results of printed specimens (a) grid, (b) hexagonal and (c) concentric infill patterns.

of 39.3 MPa at both 80% and 100% infill with 200 °C. These results align with the study of [50], who noted that hexagonal patterns provide an efficient balance between weight reduction and structural integrity. However, a performance plateau beyond 80% infill suggests diminishing returns on strength as density increases further, in agreement with findings by [51].

For the concentric pattern (Fig. 6 (1c)), the tensile strength varied more significantly with changing parameters. The highest strength value of 38.6 MPa was achieved at 200 °C and 100% infill. The increased variability may be attributed to the directional nature of concentric infill structures, which was similarly observed by [52], who reported that anisotropic infill geometries lead to inconsistent mechanical responses under tensile loading.

The modulus of elasticity followed trends similar to those observed in tensile strength (Fig. 6 (2)). The grid pattern produced the highest modulus value of 3045 MPa (215 °C, 100% infill), followed by 2722 MPa (200 °C, 100% infill). These values are consistent with literature reports, such as [53], who highlighted that denser, orthogonal patterns enhance stiffness due to continuous load paths.

In the hexagonal pattern, modulus values peaked at 2945 MPa, which is slightly lower than grid values but still significant. As noted by [54], hexagonal structures distribute stress efficiently and may yield slightly more flexible but durable parts, especially under dynamic loads.

The concentric pattern demonstrated a peak modulus of 3013 MPa yet showed the widest fluctuation range across different parameters (1870–3013 MPa). This outcome may be explained by the layer-wise directional bonding, which is more vulnerable to print-induced defects and inconsistencies [55].

Comparative analysis shows that grid-patterned specimens consistently outperformed the others in both strength and stiffness. This agrees with the work of [56], who demonstrated the superiority of rectilinear patterns for structural applications. The hexagonal pattern, though slightly inferior in terms of absolute values, offers a favorable balance of strength and material efficiency, confirming its suitability for applications prioritizing weight reduction. Concentric patterns, while capable of achieving high mechanical properties, are more susceptible to variations in processing conditions, as suggested by [57].

These findings reinforce the widely accepted view that mechanical performance in FDM-printed PLA parts is highly dependent on the interplay between geometric design and processing parameters. Specifically, using higher infill densities (≥80%) and moderate-to-high printing temperatures (200–215 °C) significantly improves tensile performance and stiffness, in line with trends reported across the literature [58].

The mechanical behavior of 3D-printed PLA specimens was evaluated through tensile testing, and the resulting stress-strain curves are presented in Fig. 7. These results reveal the influence of printing temperature, infill pattern, and infill density on the tensile properties of PLA.

Fig. 7(a) compares the stress-strain responses of specimens printed with 20% and 80% infill density and different infill patterns (Grid, Hexagonal, Concentric) at three temperatures: 185 °C, 200 °C, and 215 °C. Among these, the specimen 80% infill density and printed at 200 °C with a Concentric infill pattern exhibited the highest tensile strength, exceeding 35 MPa. This enhancement in tensile strength can be attributed to improved layer adhesion and reduced voids at higher extrusion temperatures [59]. The 200_Hex_20 specimen, although printed with only 20% infill, also demonstrated relatively high tensile strength, likely due to the geometric efficiency of the hexagonal pattern in distributing tensile loads.

At a fixed printing temperature of 200 °C and 100% infill density, Fig. 7(b) shows that the Hexagonal pattern outperformed both Grid and Concentric patterns in terms of ultimate tensile strength, reaching nearly 39 MPa. The variation in tensile strength among the printed specimens can be explained by the combined effects of polymer chain diffusion, interlayer bonding quality, and void distribution. At higher extrusion

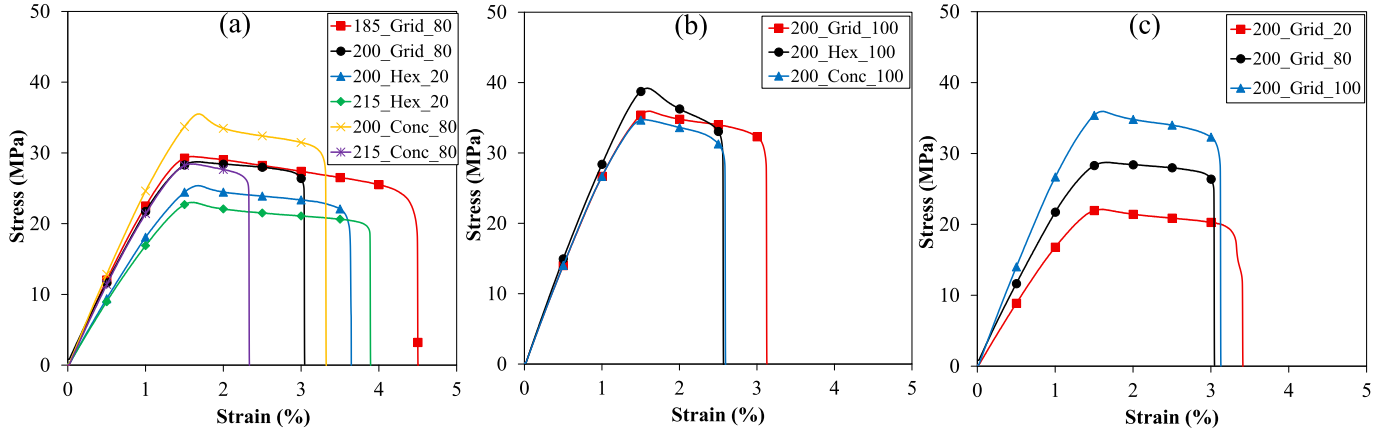

Fig. 7. Stress-strain curves of PLA specimens.

temperatures, the molecular mobility of PLA chains increases, promoting interlayer diffusion and stronger weld formation at the interface of adjacent filaments. This leads to improved stress transfer and higher tensile strength. Conversely, at lower extrusion temperatures, insufficient chain mobility results in poor interfacial adhesion and the formation of weak boundary zones between layers. Moreover, infill pattern also affects the load transfer path—grid and hexagonal structures provide multidirectional stress distribution, while concentric paths offer better circumferential bonding but reduced axial strength. Therefore, the mechanical performance of FDM-printed PLA is governed by the balance between thermal energy input and interlayer molecular diffusion during deposition. This observation aligns with previous research indicating that hexagonal infill provides isotropic load distribution and improved stress transfer capabilities [60]. While the Grid and Concentric patterns yielded comparable strength values, the concentric pattern again displayed slightly higher strain at break, suggesting a trade-off between strength and ductility depending on the infill pattern used.

The third set of curves Fig. 7(c) illustrates the stress-strain behavior of Grid-patterned specimens printed at 200 °C with varying infill densities (20%, 80%, 100%). As expected, tensile strength increased with infill density. The 200_Grid_20 specimen exhibited the lowest strength (~23 MPa) and strain capacity, while the 200_Grid_100 sample showed significantly improved tensile properties (~36 MPa). The increase in strength is directly related to the increased material volume and internal continuity of the fully dense structure, which enhances stress-bearing capacity [53].

In general, hardness values increased with higher infill density and optimized printing temperatures, showing a strong correlation between internal structure and surface resistance (Fig. 8). In the grid pattern (Fig. 8(a)), the hardness increased significantly from 64.3 (200_Grid_20) to a peak value of 81.9 (215_Grid_100). This increase can be attributed to the denser material distribution and enhanced thermal bonding between layers at elevated temperatures and higher infill. The uniform grid structure likely offers consistent resistance to indentation across the surface. These results align with previous studies, which reported that increasing infill percentage contributes to increased hardness in FDM-printed PLA materials due to improved internal support and reduced void ratio [45,48].

The hexagonal pattern (Fig. 8(b)) exhibited a similar trend, with hardness values ranging from 67.3 to 80.3 Shore-D. Although the pattern is structurally efficient, it appears slightly less effective in distributing load uniformly compared to the grid configuration, possibly due to increased anisotropy along stress paths. Nonetheless, samples with 80% and 100% infill displayed near-maximum hardness values, consistent with results from [49], who reported higher hardness values in denser and more geometrically compact structures.

For the concentric pattern (Fig. 8(c)), hardness values were relatively higher overall, ranging from 65.9 to 82.7 Shore-D. The specimen 200_Conc_100 showed the highest recorded hardness (82.7) among all tested configurations. This may be attributed to the circular layering path, which increases bonding perimeter and load dispersion. Previous research has noted the advantage of concentric infill in enhancing mechanical performance due to its continuous extrusion path, which minimizes discontinuities and stress concentration points [55].

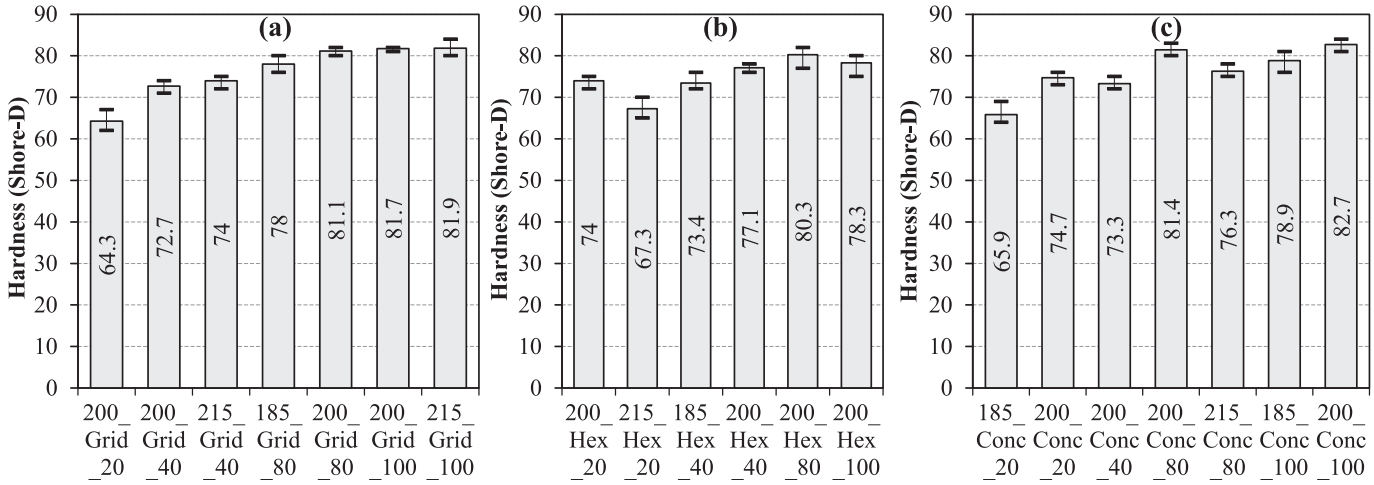

Fig. 8. Hardness test results of printed specimens (a) grid, (b) hexagonal and (c) concentric infill patterns.

In all patterns, lower infill densities (20% and 40%) consistently resulted in reduced hardness, highlighting the critical role of internal material support in resisting indentation. Moreover, the influence of printing temperature is evident, as samples printed at 215 °C generally performed better than those at lower temperatures (185 °C or 200 °C), supporting findings by [56], who emphasized the impact of extrusion temperature on inter-layer adhesion and mechanical integrity. The increase in Shore D hardness with higher printing temperature can be attributed to enhanced polymer chain diffusion and inter-layer fusion, which reduce micro-voids and improve molecular entanglement at the interfaces. Additionally, the infill pattern influences stress distribution and load transfer efficiency; for instance, the grid and concentric configurations promote more continuous bonding paths that limit localized stress concentrations. Consequently, the synergistic effects of thermal consolidation and geometric continuity explain the superior hardness observed at 215 °C and higher infill densities, as also supported by previous studies that highlighted the influence of extrusion temperature and interlayer bonding on the mechanical behavior of FDM-printed PLA [50,53,56]. Overall, the concentric pattern with 100% infill at 200 °C provided the highest hardness, suggesting that for applications where surface durability and indentation resistance are critical, this configuration may be preferred.

3.2. Fractographic analysis

Fig. 9 presents digital microscope images of fractured PLA specimens fabricated with different infill geometries, extrusion temperatures, and infill densities. The fracture surface morphology provides insights into the failure mechanisms, interlayer bonding, and structural continuity of the FDM-printed components. Among all geometries, grid-patterned specimens display the clearest relationship between infill density and fracture morphology. The 200_Grid_20 specimen reveals an irregular, porous fracture surface with visible interlayer gaps, reflecting insufficient structural continuity and weak interfacial strength. In contrast, the 200_Grid_100 specimen shows a compact, homogeneous surface, indicating strong mechanical interlocking and consistent load-bearing capacity. Increasing the extrusion temperature from 185 °C to 200 °C, as seen in the 185_Grid_80 and 200_Grid_80 specimens, results in more cohesive fracture structures, demonstrating improved thermal bonding between layers. These observations confirm that the grid pattern, particularly at full density and elevated temperatures, enhances both structural integrity and energy absorption under tensile loading.

Hexagonal infill geometries exhibit more uniform and isotropic fracture behavior. The 200_Hex_20 and 215_Hex_20 specimens show relatively even crack propagation paths, despite their low infill ratios. The geometric efficiency of the hexagonal layout appears to enable better stress distribution, reducing localized strain concentrations. At 100% infill, the 200_Hex_100 specimen presents a smooth, continuous fracture surface with multiple microcrack branches. These patterns suggest stable failure mechanisms and superior energy dissipation capabilities. Compared to grid structures, hexagonal infill provides slightly lower absolute stiffness but offers greater mechanical efficiency through optimized material usage and more balanced load transmission.

Concentric infill specimens demonstrate highly directional fracture morphologies aligned with the circular deposition paths. The 200_Conc_80 and 215_Conc_80 samples reveal linear fracture traces following the concentric pattern, indicating anisotropic load response. The 215_Conc_80 specimen, produced at higher temperature, shows enhanced layer adhesion but also exhibits a more brittle fracture surface, likely due to increased stiffness. At 100% infill, the 200_Conc_100 sample presents a continuous yet directionally aligned surface, reflecting strong bonding along the print path but reduced crack deflection capability compared to the hexagonal pattern. Although concentric infill results in the highest surface hardness, it introduces fracture anisotropy, which may influence performance under multi-axial loading conditions. In summary, the fractographic analysis highlights the critical influence

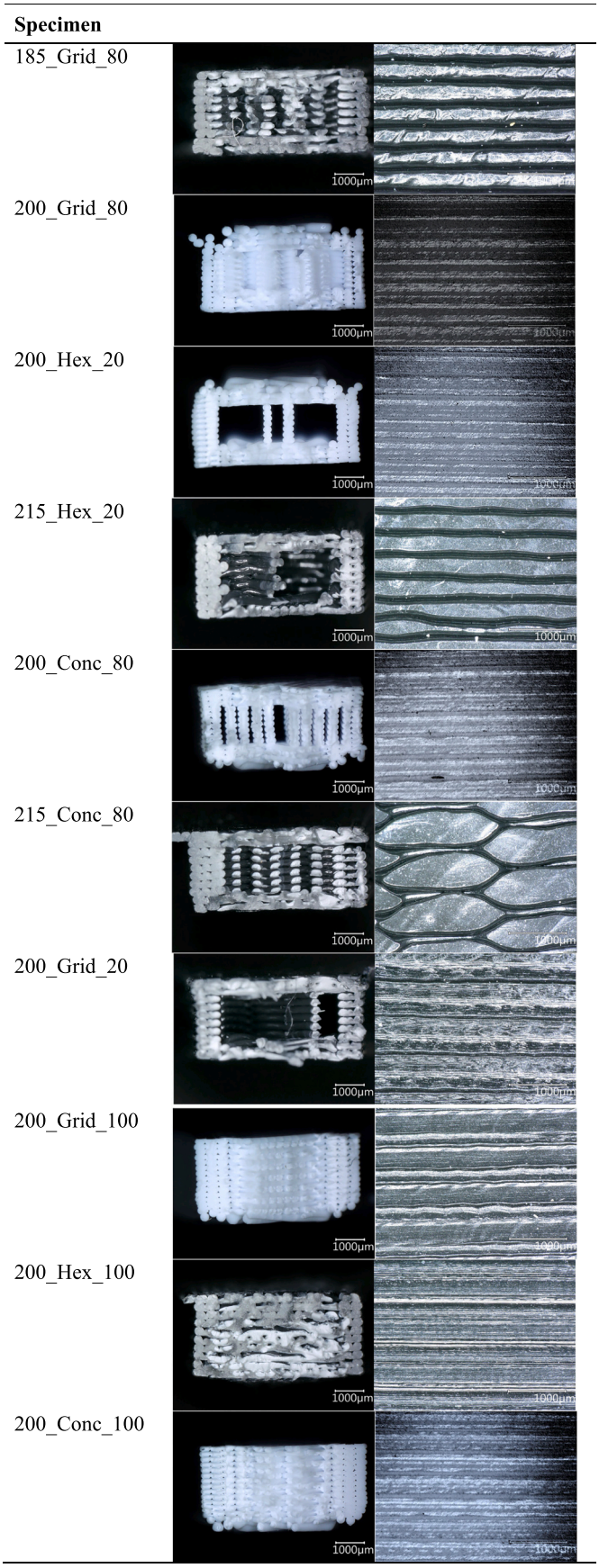

Fig. 9. Fracture surfaces and specimen surfaces of tensile test specimens.

of internal architecture on the failure characteristics of PLA parts. Grid infill enhances stiffness and strength through dense interlayer contact. Hexagonal infill provides balanced mechanical performance with efficient material use and isotropic failure behavior. Concentric infill improves surface quality and layer cohesion but induces directional fracture tendencies. These findings highlight the critical role of choosing suitable infill strategies in accordance with the desired mechanical performance and functional requirements of the printed component.

3.3. Drilling thrust forces

In the machining study, the thrust force generated during drilling of FDM-manufactured PLA specimens was examined under different processing conditions. Drilling experiments were carried out using a CNC milling machine, employing spindle speeds of 1500 and 3000 rpm and feed rates of 150 and 300 mm/min. The thrust forces corresponding to each parameter set are summarized in Table 8 and illustrated in Fig. 10, with Fig. 10(a) and (b) showing the results at 1500 rpm and 3000 rpm, respectively.

Overall, higher feed rates consistently led to increased thrust forces, a trend commonly reported in polymer machining due to the larger uncut chip thickness and reduced tool–material interaction time, which intensify cutting severity. For example, at 1500 rpm, the 185_Grid_80 specimen recorded a thrust force of 65.4 N at 150 mm/min, which rose to 80.1 N at 300 mm/min. This observation aligns with previous findings in polymer drilling, where increasing the feed rate correlates with higher cutting resistance [61].

The influence of infill pattern and density was also evident. Among all configurations, specimens with 20% hexagonal infill (Hex_20) exhibited the lowest thrust forces across both spindle speeds, indicating reduced material resistance to drilling. In contrast, concentric-patterned specimens with 80% infill (Conc_80) produced the highest thrust forces, particularly under the most severe cutting condition (3000 rpm, 300 mm/min). This highlights the combined effect of material quantity and infill orientation on drilling resistance. At 200 °C, the hexagonal pattern further demonstrated advantages, yielding lower thrust forces (62.2 N at 150 mm/min and 55.5 N at 300 mm/min) compared to grid and concentric patterns, likely due to its superior load distribution and reduced cross-sectional area resisting the tool [59]. The variation in drilling response among the printed specimens can be attributed to the combined effects of thermal softening, frictional heating, and anisotropic layer orientation. When the local temperature approaches the glass transition point of PLA, the polymer matrix undergoes viscoelastic deformation and partial re-melting, reducing its resistance to cutting and promoting chip adhesion along the hole wall. This thermally softened region, together with frictional heat accumulation and insufficient chip evacuation, leads to surface degradation and burr formation. Conversely, at lower temperatures, inadequate interlayer fusion and increased brittleness cause microcracking and irregular chip removal at filament interfaces. Additionally, the drilling direction relative to the filament deposition path affects the effective cutting angle, generating fluctuating thrust forces and non-uniform surface morphology. Hence, the interplay between heat generation, interlayer adhesion, and viscoelastic softening governs the overall drilling behavior and machined surface integrity of FDM-printed PLA parts.

Table 8
Thrust force (N) values of PLA specimens obtained experimentally and numerically.

Specimen	Spindle speed (rpm)–feed rate (mm/min)			
	1500–150	1500–300	3000–150	3000–300
185_Grid_80	65.4 ± 1.0	80 ± 1.7	55.7 ± 0.6	65.9 ± 0.4
200_Grid_80	69 ± 2.6	75.3 ± 0	52 ± 0.4	72.6 ± 1.9
200_Hex_20	62.2 ± 2.5	62 ± 1.5	55.5 ± 0.9	51.5 ± 3.4
215_Hex_20	42.7 ± 1.0	51 ± 0.3	42.8 ± 0.9	44.2 ± 2.5
200_Conc_80	69 ± 1.8	75.8 ± 0.4	64.1 ± 0.4	68.5 ± 3.0
215_Conc_80	65.8 ± 1.2	73.1 ± 2.3	54.1 ± 1.2	63.6 ± 0.8
200_Grid_20	51.4 ± 2.7	56.6 ± 1.1	42.9 ± 0.2	50.8 ± 3.9
200_Grid_100	75.1 ± 0.1	90.6 ± 0.8	64.1 ± 1.5	79.5 ± 0.6
200_Hex_100	58.7 ± 2.9	62.1 ± 0.7	60.1 ± 1.2	52.1 ± 1.5
200_Conc_100	71 ± 1.0	89 ± 1.9	93.3 ± 4.2	84 ± 5.6
Average	63.03 ± 0.60	71.55 ± 0.41	58.46 ± 0.50	63.27 ± 0.90
FE simulations	68.23	82.83	62.08	72.89
Diff between tests and FE simulation (%)	8.25	15.76	6.19	15.20

FE simulations were conducted to provide additional insight into the deformation response of PLA during drilling. The comparison between the experimental and numerical thrust force results (Table 8) indicates that the FE simulations generally overpredict the thrust force values compared to experimental measurements, with deviations ranging from 6.19% to 15.76%. The smallest discrepancy was observed at 3000 rpm–150 mm/min (6.19%), whereas the largest difference occurred at 1500 rpm–300 mm/min (15.76%). This trend suggests that the model successfully captures the overall influence of spindle speed and feed rate on thrust force, though it slightly overestimates the absolute force levels.

These differences can be attributed to several factors. First, in the numerical model, idealized boundary and contact conditions were assumed, disregarding minor vibrations, tool run-out, and transient thermal fluctuations that naturally occur during drilling. Second, the Hashin damage model used to represent the material behavior assumes uniform damage initiation and progression based on homogenized composite failure criteria. However, in reality, FDM-printed PLA exhibits layer-dependent failure modes influenced by interlayer bonding quality and micro-void distribution, which the Hashin model may not fully capture under localized drilling-induced stresses and strain gradients. Additionally, the frictional contact between the drill bit and the workpiece was modeled using a constant coefficient, while in experiments, friction varies dynamically with temperature rise, chip formation, and surface softening. Moreover, microstructural heterogeneities and residual porosity inherent to FDM parts contribute to localized compliance and deformation behavior that cannot be precisely represented in the FE mesh. Nevertheless, the relatively low deviation (<16%) confirms that the developed simulation framework offers a robust and predictive approximation of the thrust force response across the investigated machining conditions.

As shown in Table 8, doubling the feed rate from 150 mm/min to 300 mm/min increased the thrust force predicted by FE simulations by 21.38% (from 68.23 N to 82.83 N) at 1500 rpm and by 17.41% (from 62.08 N to 72.89 N) at 3000 rpm. This increase in thrust force with higher feed rates is attributed to the larger uncut chip thickness and higher material removal per revolution, which elevate cutting resistance and intensify tool–workpiece interactions, thereby requiring greater force to maintain chip formation and tool penetration.

When the spindle speed was increased to 3000 rpm, the thrust forces slightly decreased across most specimens, attributed to improved thermal softening and chip evacuation at higher cutting speeds [62]. Nevertheless, the concentric infill pattern maintained relatively higher thrust force values compared to others, indicating greater structural continuity and stiffness in the drilling axis.

A clear positive correlation was observed between infill density and thrust force. As shown in Fig. 10c to f, specimens with 100% infill exhibited significantly higher thrust forces across all feed rates. For instance, the 200_Grid_100 specimen showed thrust forces of 75.1 N and 90.6 N at 150 and 300 mm/min feed rates, respectively. This increase is expected, as higher infill provides more material resistance, requiring greater force for tool penetration [63].

Under the highest feed rate condition (3000−300), the 200_Conc_100 specimen demonstrated the highest thrust force value (84.0 ± 5.6 N), confirming that both infill pattern and density significantly influence cutting resistance. Notably, among fully dense samples, Grid and Concentric patterns consistently led to higher thrust forces compared to Hexagonal, suggesting that internal geometry plays a

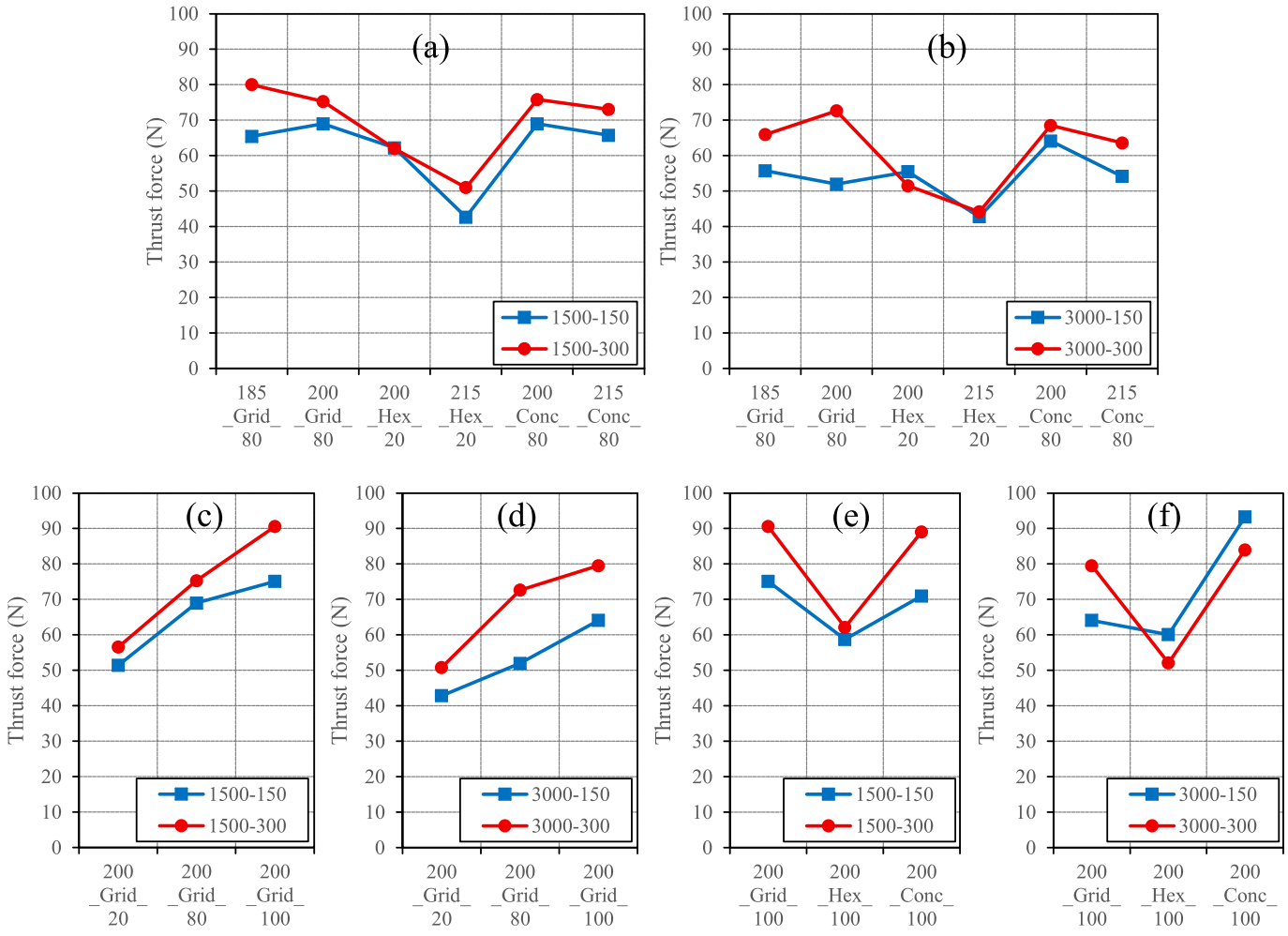

Fig. 10. Thrust force graphs of PLA specimens.

critical role in tool-material interaction during drilling.

3.4. Hole quality and delamination analysis

The digital microscope images of the drilled holes on PLA specimens produced via fused deposition modeling (FDM), following CNC drilling under various spindle speed and feed rate conditions presented in Fig. 11. The analysis reveals that the hole quality, including edge regularity, burr formation, and surface cleanliness, is highly sensitive to both the printing parameters and the drilling conditions.

In almost all cases, increasing the feed rate from 150 mm/min to 300 mm/min led to a noticeable decrease in hole quality, as shown by the presence of increased burrs, delamination, and edge chipping. This was particularly evident in samples processed at 1500 rpm–300 mm/min and 3000 rpm–300 mm/min, where the higher thrust forces likely induced mechanical stresses that exceeded the local inter-layer adhesion strength. By contrast, lower feed rates (150 mm/min) generally produce cleaner hole edges with minimal material damage, indicating more stable cutting and lower heat generation. Fig. 12 presents the numerically obtained CSDMG distribution, illustrating the extent of delamination within the interface layer located 2 mm beneath the drilled surface of the PLA plate under various drilling conditions. The areas shaded in gray correspond to regions with a scalar damage value greater than 0.9, indicating severe delamination (a value of 1.0 denotes complete delamination). This visual evidence is further supported by the quantitative results summarized in Table 6, which lists the delamination factor for each case. The variation in delamination behavior among FDM-printed PLA specimens can be explained by the combined effects of interlayer adhesion, thermal softening, and stress redistribution near the hole exit. At higher feed rates, increased chip load and frictional heating induce local interlaminar stresses that exceed the weak bonding strength between deposited layers, promoting layer separation and burr formation. Conversely, at higher spindle speeds, improved heat dissipation and reduced thrust forces limit this stress accumulation, resulting in smoother hole boundaries. Additionally, higher infill densities increase local stiffness but restrict heat dissipation, which intensifies delamination at elevated feed rates. Therefore, the delamination response is governed by the balance between mechanical loading and thermal relaxation during the drilling process, which controls the integrity of interlayer bonding and the extent of interfacial damage. It was observed that increasing the feed rate from 150 mm/min to 300 mm/min, while maintaining a constant spindle speed of 1500 rpm, caused a noticeable expansion of the delaminated zone, with DF rising from 1.68 to 2.06. This trend corresponds well with the experimental observations, confirming that higher feed rates intensify material damage near the hole exit due to increased thrust forces (rising from 62.08 N to 72.89 N for the respective cases, see Table 8) and elevated stress concentrations within the interface layer [64,65].

Higher spindle speeds (3000 rpm) were observed to reduce burr formation and improve edge regularity in some configurations, likely due to improved chip evacuation and reduced cutting time. The numerical results shown in Fig. 12 indicate that increasing the spindle speed from 1500 rpm to 3000 rpm, while keeping the feed rate constant at 150 mm/min, led to a marked reduction in the delaminated region,

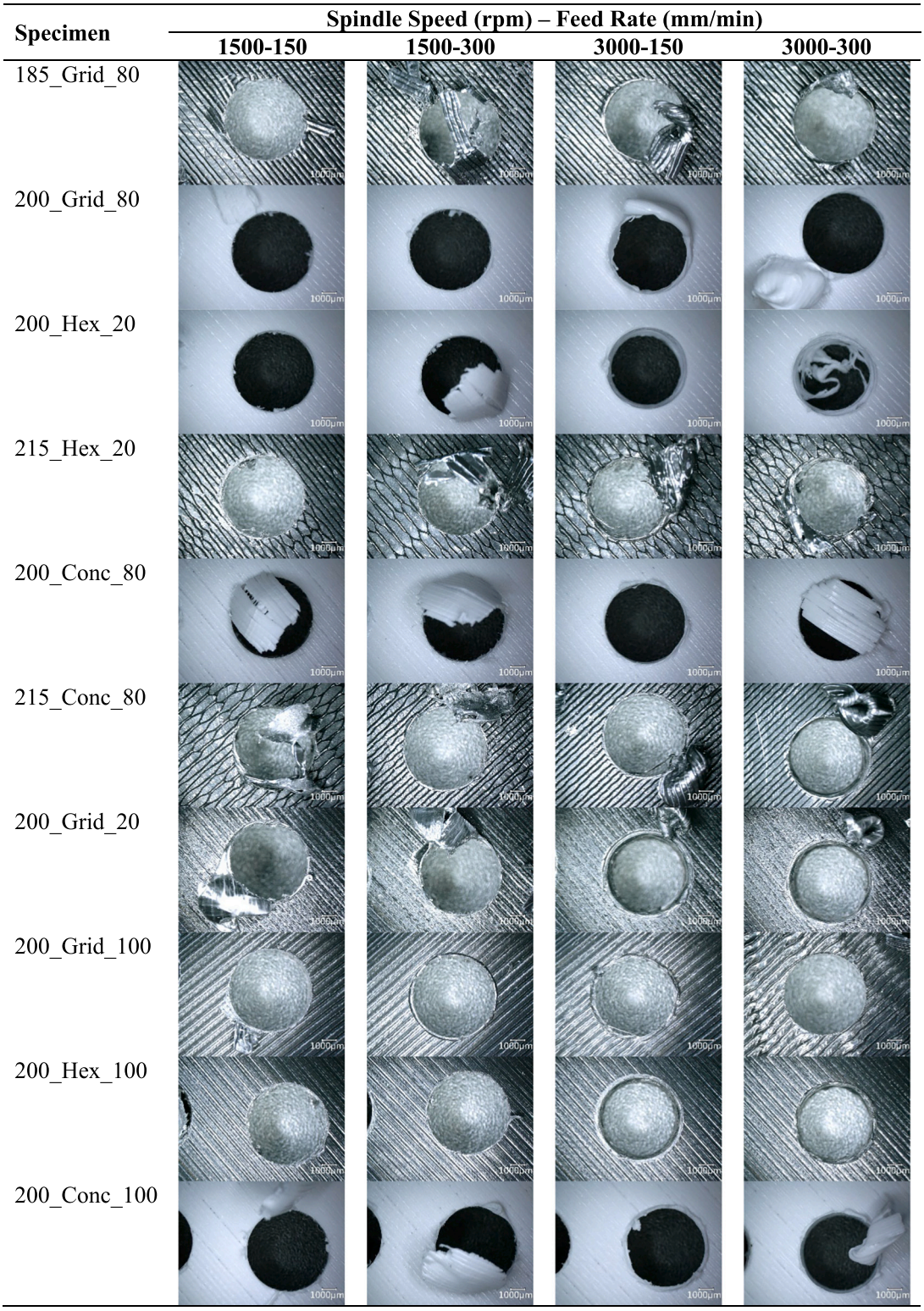

Fig. 11. The digital microscope images of the drilled holes on PLA specimens.

with the *DF* decreasing from 2.63 to 1.68 (see Table 9). This improvement can be attributed to the enhanced cutting efficiency and lower thrust forces at higher spindle speeds (decreasing from 68.23 N to 62.08 N, see Table 8), which promote smoother material removal and reduce stress concentrations around the hole boundary. As a result, the interlayer region experienced less mechanical disruption, thereby minimizing delamination [66]. These findings are in close agreement with the experimental results, reinforcing the accuracy of the numerical model in capturing the influence of spindle speed on drilling-induced damage mechanisms in PLA composites. On the other hand, however, the tests demonstrated that at high spindle speed combined with high feed rate, thermal softening and plastic deformation around the hole periphery became more evident, particularly in high-density specimens. The hole quality variation in FDM-printed PLA can be interpreted in

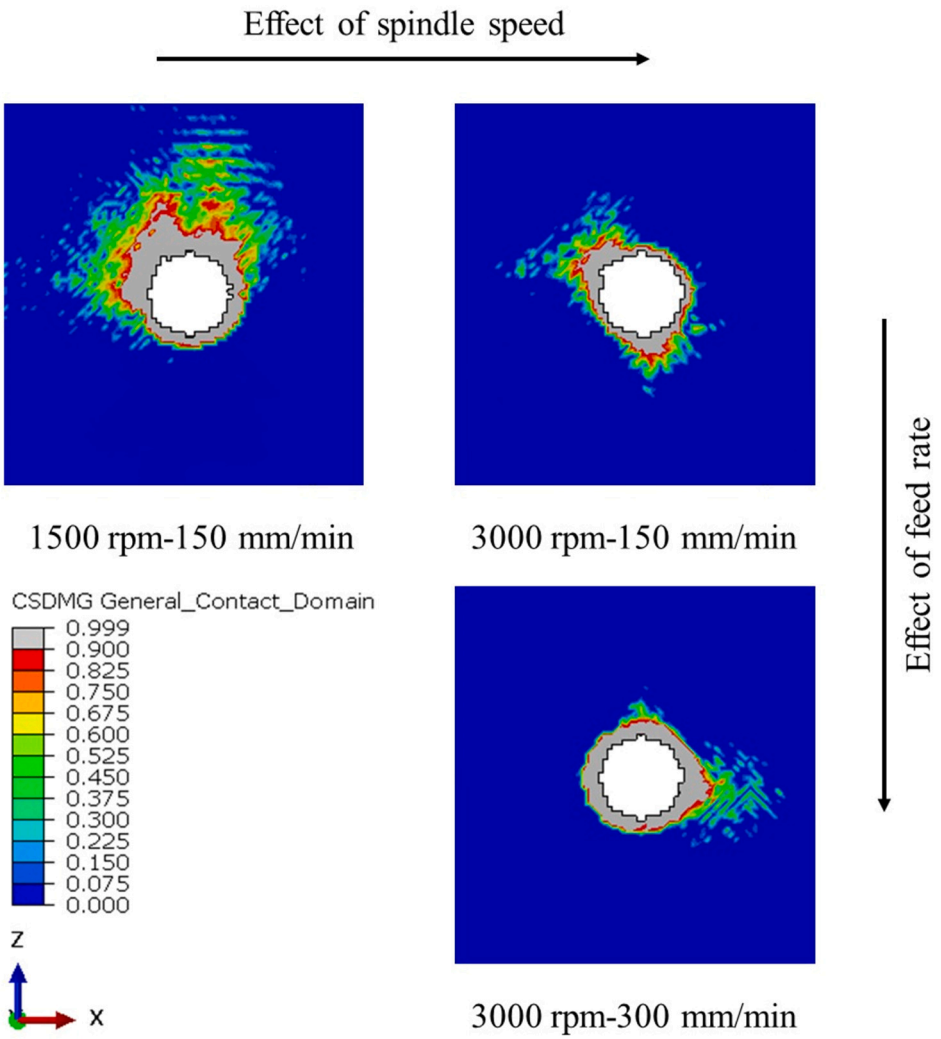

Fig. 12. The degree of delamination—indicated by the CSDMG distribution—along the interface layer located 2 mm beneath the drilled surface of the PLA plate under different drilling conditions (within a 40 mm × 40 mm region shown).

Table 9
Numerically obtained *DF* values from the drilling of PLA plate for different configurations.

	Feed rate (mm/min)	Spindle speed (rpm)	*DA* (mm^2)	*NA* (mm^2)	*DF*
1	150	1500	74.35	28.27	2.63
2	150	3000	47.49	28.27	1.68
3	300	3000	58.23	28.27	2.06

terms of localized thermal–mechanical interactions during drilling. At elevated spindle speeds, the frictional heat generated between the cutting edge and softened PLA matrix promotes partial melting and polymer smearing along the hole wall, reducing surface roughness but deteriorating dimensional accuracy. Conversely, at lower speeds, the limited thermal softening and brittle fracture of interlayer bonds result in micro-chipping and rougher hole edges. Furthermore, high feed rates intensify plastic deformation and induce material pull-out due to insufficient chip evacuation. The anisotropic layer orientation also influences the effective cutting angle, leading to uneven surface finish along the layer boundaries. Hence, the final surface integrity is governed by the competition between heat-assisted viscoplastic flow and mechanically induced fracture, which together determine the smoothness and accuracy of the drilled holes. The extent of the heat-affected zone around the drilled holes also depends on the combined influence of spindle speed and feed rate, where excessive localized heating promotes re-melting and surface deterioration.

In some high-feed, high-density, and moderate-temperature samples (e.g., 200_Grid_80 at 1500–300 and 3000–300), material melting, re-solidification is evident. This suggests that localized heating due to insufficient cooling and high friction may degrade the thermoplastic matrix, particularly in tightly packed structures.

From a practical design perspective, these findings provide clear guidance for engineers planning post-processing operations such as drilling. When dimensional accuracy and hole integrity are critical, selecting a hexagonal infill pattern with an optimized density can reduce machining-induced damage without excessively compromising mechanical strength. Conversely, for load-bearing components where high stiffness is required, higher infill densities and grid patterns may be preferred, but drilling parameters must be carefully controlled to avoid delamination and thermal degradation. Overall, the results emphasize the importance of co-designing printing parameters and machining conditions to achieve a balanced trade-off between structural performance and manufacturability in FDM-fabricated components.

4. Conclusions

This study comprehensively investigated the mechanical and machining performance of FDM-printed PLA parts, focusing on the

effects of infill pattern (grid, hexagonal, concentric), infill density, and printing temperature. The combined experimental and numerical analyses yielded several key insights that can guide the optimization of additive manufacturing parameters for structural and functional applications:

- Infill density was the most dominant factor influencing tensile strength, stiffness, and hardness. Increasing infill from 20% to 100% consistently enhanced all mechanical properties due to improved internal bonding and structural continuity. Fully dense samples (100% infill) exhibited the highest load-bearing capacity but also higher thrust forces during drilling, reflecting greater material resistance.
- The grid pattern delivered the best overall mechanical performance, achieving a tensile strength of 40.3 MPa and a modulus of 3050 MPa at 100% infill and 215 °C. The hexagonal pattern, though slightly less stiff, provided good strength-to-weight efficiency, making it suitable for lightweight applications. The concentric pattern showed high surface hardness (82.7 Shore D at 100% infill and 200 °C) and good wear resistance but was more sensitive to variations in process parameters.
- Higher printing temperatures (200–215 °C) enhanced interlayer bonding and polymer flow, improving tensile strength and stiffness compared to parts printed at lower temperatures (185 °C). Elevated temperatures also contributed to improved dimensional consistency and reduced internal voids.
- Drilling tests revealed that thrust force increased with infill density and stiffness, especially for grid-patterned specimens. Lower infill densities and hexagonal patterns facilitated smoother drilling with reduced cutting forces and minimal thermal/mechanical damage. Both microscopic observations and FE simulations confirmed that low feed rates and moderate-to-high spindle speeds are optimal for maintaining hole integrity in FDM-printed PLA parts.
- For applications demanding high strength and stiffness, a grid infill pattern, 100% density, and printing temperatures of 200–215 °C are recommended. For lightweight or machinable components, the hexagonal infill at moderate density offers an effective balance between mechanical performance and ease of post-processing. The results emphasize the importance of aligning printing parameters with post-processing needs to ensure mechanical reliability and surface quality in polymer additive manufacturing.

Building upon the present findings, future research could be directed toward exploring a broader range of thermoplastic polymers, such as ABS, PETG, or high-performance composites reinforced with short or continuous fibers, to evaluate how their distinct thermal and rheological behaviors influence both mechanical and machining responses. Additionally, investigating hybrid or functionally graded infill architectures—combining multiple patterns or variable densities within a single part—could offer improved performance-to-weight ratios and localized optimization for specific loading or machining conditions. Beyond material and geometric considerations, the effects of process-related factors such as active cooling strategies, ambient temperature control, and tool geometry (e.g., point angle, helix angle, and coating) on drilling-induced damage, thermal gradients, and surface finish should be systematically analyzed. These extensions would not only deepen the understanding of process–structure–property relationships in polymer additive manufacturing but also provide a robust foundation for developing predictive models and adaptive parameter selection strategies tailored to diverse engineering applications.

CRediT authorship contribution statement

Uğur Köklü: Writing – review & editing, Validation, Methodology, Investigation, Conceptualization. **Levent Urtekin:** Writing – review & editing, Validation, Methodology, Investigation, Conceptualization. **Erkin Akdoğan:** Writing – review & editing, Validation, Methodology, Investigation, Conceptualization. **Faik Yılan:** Writing – review & editing, Writing – original draft, Methodology, Investigation. **Murat Demiral:** Writing – original draft, Validation, Software, Methodology, Investigation.

Declaration of competing interest

The authors declare that they have no known competing financial interests or personal relationships that could have appeared to influence the work reported in this paper.

References

[1] Gibson I, Rosen DW, Stucker B. Chapter 6 Extrusion-Based Systems. 2010.
[2] Singh S, Ramakrishna S, Singh R. Material issues in additive manufacturing: a review. J Manuf Process 2017;25:185–200. https://doi.org/10.1016/j.jmapro.2016.11.006.
[3] Srivastava M, Rathee S, Patel V, Kumar A, Koppad PG. A review of various materials for additive manufacturing: recent trends and processing issues. J Mater Res Technol 2022;21:2612–41. https://doi.org/10.1016/j.jmrt.2022.10.015.
[4] Altıparmak SC, Xiao B. A market assessment of additive manufacturing potential for the aerospace industry. J Manuf Process 2021;68:728–38.
[5] Bhadeshia HKDH. Additive manufacturing. Mater Sci Technol (United Kingdom) 2016;32:615–6. https://doi.org/10.1080/02670836.2016.1197523.
[6] Coakley M, Hurt DE. 3D printing in the laboratory: maximize time and funds with customized and open-source labware. J Lab Autom 2016;21:489–95. https://doi.org/10.1177/2211068216649578.
[7] Khoo ZX, Teoh JEM, Liu Y, Chua CK, Yang S, An J, et al. 3D printing of smart materials: a review on recent progresses in 4D printing. Virtual Phys Prototyp 2015;10:103–22. https://doi.org/10.1080/17452759.2015.1097054.
[8] Abdulhameed O, Al-Ahmari A, Ameen W, Mian SH. Additive manufacturing: challenges, trends, and applications. Adv Mech Eng 2019;11:1–27. https://doi.org/10.1177/1687814018822880.
[9] Oleff A, Küster B, Stonis M, Overmeyer L. Process monitoring for material extrusion additive manufacturing: a state-of-the-art review. Prog Addit Manuf 2021;6:705–30. https://doi.org/10.1007/s40964-021-00192-4.
[10] Cano-Vicent A, Tambuwala MM, Hassan SS, Barh D, Aljabali AAA, Birkett M, et al. Fused deposition modelling: current status, methodology, applications and future prospects. Addit Manuf 2021;47. https://doi.org/10.1016/j.addma.2021.102378.
[11] Mohamed OA, Masood SH, Bhowmik JL. Optimization of fused deposition modeling process parameters: a review of current research and future prospects. Adv Manuf 2015;3:42–53. https://doi.org/10.1007/s40436-014-0097-7.
[12] Ngo TD, Kashani A, Imbalzano G, Nguyen KTQ, Hui D. Additive manufacturing (3D printing): a review of materials, methods, applications and challenges. Compos Part B Eng 2018;143:172–96. https://doi.org/10.1016/j.compositesb.2018.02.012.
[13] Rajan K, Samykano M, Kadirgama K, Harun WSW, Rahman MM. Fused deposition modeling: process, materials, parameters, properties, and applicationsvol. 120. Springer London; 2022. https://doi.org/10.1007/s00170-022-08860-7.
[14] Nurhudan AI, Supriadi S, Whulanza Y, Saragih AS. Additive manufacturing of metallic based on extrusion process: a review. J Manuf Process 2021;66:228–37.
[15] Orisekeh DK, Corti G, Jahan MP. Enhancing thermo-mechanical properties of additively manufactured PLA using eggshell microparticle fillers. J Manuf Process 2025;133:782–97.
[16] Yao T, Ye J, Deng Z, Zhang K, Ma Y, Ouyang H. Tensile failure strength and separation angle of FDM 3D printing PLA material: experimental and theoretical analyses. Compos Part B Eng 2020;188:107894. https://doi.org/10.1016/j.compositesb.2020.107894.
[17] Behzadnasab M, Yousefi AA, Ebrahimibagha D, Nasiri F. Effects of processing conditions on mechanical properties of PLA printed parts. Rapid Prototyp J 2020;26:381–9. https://doi.org/10.1108/RPJ-02-2019-0048.
[18] Gonabadi H, Yadav A, Bull SJ. The effect of processing parameters on the mechanical characteristics of PLA produced by a 3D FFF printer. Int J Adv Manuf Technol 2020;111:695–709. https://doi.org/10.1007/s00170-020-06138-4.
[19] Yilan F, Şahin İB, Koç F, Urtekin L. The effects of different process parameters of PLA+ on tensile strengths in 3D printer produced by fused deposition modeling. El-Cezeri J Sci Eng 2023;10:160–73. https://doi.org/10.31202/ecjse.1179492.
[20] Vălean C, Baban M, Rajak DK, Linul E. Effect of multiple process parameters on optimizing tensile properties for material extrusion-based additive manufacturing. Construct Build Mater 2024;414. https://doi.org/10.1016/j.conbuildmat.2024.135015.
[21] Vălean C, Linul E, Palomba G, Epasto G. Single and repeated impact behavior of material extrusion-based additive manufactured PLA parts. J Mater Res Technol 2024;30:1470–81. https://doi.org/10.1016/j.jmrt.2024.03.150.
[22] Dey A, Yodo N. A systematic survey of FDM process parameter optimization and their influence on part characteristics. J Manuf Mater Process 2019;3. https://doi.org/10.3390/jmmp3030064.
[23] Beniak J, Šooš L, Križan P, Matúš M, Ruprich V. Resistance and strength of conductive PLA processed by FDM additive manufacturing. Polymers (Basel) 2022;14. https://doi.org/10.3390/polym14040678.

[24] Jaisingh Sheoran A, Kumar H. Fused deposition modeling process parameters optimization and effect on mechanical properties and part quality: review and reflection on present research. Mater Today Proc 2020;21:1659–72. https://doi.org/10.1016/j.matpr.2019.11.296.
[25] Pratama J, Cahyono SI, Suyitno S, Muflikhun MA, Salim UA, Mahardika M, et al. A review on reinforcement methods for polymeric materials processed using fused filament fabrication (FFF). Polymers (Basel) 2021;13:1–23. https://doi.org/10.3390/polym13224022.
[26] Equbal A, Akhter S, Equbal MA, Sood AK. Application of machine learning in fused deposition modeling: a review. 2021. https://doi.org/10.1007/978-3-030-68024-4_23.
[27] Ujeniya PS, Rachchh NV. A review on manufacturing, machining, and recycling of 3D printed composite materials. IOP Conf Ser Mater Sci Eng 2019:653. https://doi.org/10.1088/1757-899X/653/1/012024.
[28] Batista M, Piñero D, Ramírez M, Mayuet PF, Bienvenido R, Vazquez JM. Defectology characterization of FDM drilled parts. IOP Conf Ser Mater Sci Eng 2021;1193:012054. https://doi.org/10.1088/1757-899X/1193/1/012054.
[29] Lalegani Dezaki M, Mohd Ariffin MK, Baharuddin BT. Experimental study of drilling 3D printed polylactic acid (PLA) in FDM process. In: InFused Deposition Modeling Based 3D Printing. Cham: Springer International Publishing; 2021 Apr 22. p. 85–106.
[30] Madhan Kumar A, Jayakumar K. Mechanical and drilling characterization of biodegradable PLA particulate green composites. J Chinese Inst Eng Trans Chinese Inst Eng A 2022;45:437–52. https://doi.org/10.1080/02533839.2022.2061602.
[31] Ulkir O. Investigation on the mechanical and thermal properties of metal-PLA composites fabricated by FDM. Rapid Prototyp J 2024;30(10):2113–22.
[32] Ozkul M, Kuncan F, Ulkir O. Predictive modeling of additively manufactured carbon fiber-PLA mechanical components via ML. Multidiscip Model Mater Struct 2025;21(5):1092–110.
[33] Baraheni M, Shabgard MR, Amini S, Gholipour F. Experimental evaluation and optimization of parameters affecting delamination, geometrical tolerance and surface roughness in ultrasonic drilling of 3D-printed PLA thermoplastic. J Thermoplast Compos Mater 2024:08927057241264803.
[34] Shunmugesh K, Ganesh M, Bhavani R, Khan MA, Saravana Kumar M, Rajeshkumar L, et al. Enhancing drilling performance in 3D printed PLA implants application of PIV and ML models. Sci Rep 2025;15(1):13314.
[35] Adanur Ö, Koçar O, Güldibi AS. Effect of the infill pattern on mechanical properties of PLAmaterials manufactured by FDM method. Bilecik Seyh Edebali Univ J Sci 2024;11:294–307. https://doi.org/10.35193/bseufbd.1336572.
[36] Aktürk D, Yildiz MT, Babacan N. Comparative analysis of Bcczz lattice structure compression behavior: experimental, numerical, and machine learning approaches. Int J 3D Printing Technol Digital Indus 2025;9:36–44. https://doi.org/10.46519/ij3dptdi.1490522.
[37] Ulkir O. Artificial intelligence techniques for thermomechanical property optimization of metal-PLA composites additive manufactured parts. Measurement 2025;256(A):118089. https://doi.org/10.1016/j.measurement.2025.118089.
[38] Laureto JJ, Pearce JM. Anisotropic mechanical property variance between ASTM D638-14 type i and type iv fused filament fabricated specimens. Polym Test 2018;68:294–301. https://doi.org/10.1016/j.polymertesting.2018.04.029.
[39] Gemi L, Morkavuk S, Köklü U, Gemi DS. An experimental study on the effects of various drill types on drilling performance of GFRP composite pipes and damage formation. Compos Part B Eng 2019;172:186–94. https://doi.org/10.1016/j.compositesb.2019.05.023.
[40] Boughdiri I, Mabrouki T, Zitoune R, Giasin K, Ameur MF. 3D macro-mechanical FE simulation for GLARE® drilling with experimental validation. Compos Struct 2023;304:116458. https://doi.org/10.1016/j.compstruct.2022.116458.
[41] Hashin Z. Failure criteria for unidirectional fiber composites. J Appl Mech 1980;47(2):329–34. https://doi.org/10.1115/1.3153664.
[42] Demiral M, Kadioglu F, Silberschmidt VV. Size effect in flexural behaviour of unidirectional GFRP composites. J Mech Sci Technol 2020;34(12):5053–61. https://doi.org/10.1007/s12206-020-1109-0.
[43] Yang Q, Cox B. Cohesive models for damage evolution in laminated composites. Int J Fract 2005;133(2):107–37. https://doi.org/10.1007/s10704-005-4729-6.
[44] Sabik A, Rucka M, Andrzejewska A, Wojtczak E. Tensile failure study of 3D printed PLA using DIC technique and FEM analysis. Mech Mater 2022;175:104506. https://doi.org/10.1016/j.mechmat.2022.104506.
[45] Kadioglu F, Demiral M. Failure behaviour of the single lap joints of angle-plied composites under three point bending tests. J Adhes Sci Technol 2019;34(5):531–48. https://doi.org/10.1080/01694243.2019.1674101.
[46] Simulia DS. ABAQUS 2018 User's manual. 2018 [DS SIMULIA Corp].
[47] Nazemzadeh N, Soufivand AA, Abolfathi N. Computing the bond strength of 3D printed polylactic acid scaffolds in mode I and II using experimental tests, finite element method and cohesive zone modeling. Int J Adv Manuf Technol 2022;118(7):2651–67. https://doi.org/10.1007/s00170-021-08124-w.
[48] Domingo-Espin M, Puigoriol-Forcada JM, Garcia-Granada AA, Llumà J, Borros S, Reyes G. Mechanical property characterization and simulation of fused deposition modeling polycarbonate parts. Mater Des 2015;83:670–7. https://doi.org/10.1016/j.matdes.2015.06.074.
[49] Yang C, Tian X, Liu T, Cao Y, Li D. 3D printing for continuous fiber reinforced thermoplastic composites: mechanism and performance. Rapid Prototyp J 2017;23:209–15. https://doi.org/10.1108/RPJ-08-2015-0098.
[50] Letcher T, Waytashek M. Material property testing of 3D-printed specimen in pla on an entry-level 3D printer. ASME Int Mech Eng Congr Expo Proc 2014:2A. https://doi.org/10.1115/IMECE2014-39379.
[51] Rankouhi B, Javadpour S, Delfanian F, Letcher T. Failure analysis and mechanical characterization of 3D printed ABS with respect to layer thickness and orientation. J Fail Anal Prev 2016;16:467–81. https://doi.org/10.1007/s11668-016-0113-2.
[52] Ahn SH, Montero M, Odell D, Roundy S, Wright PK. Anisotropic material properties of fused deposition modeling ABS. Rapid Prototyp J 2002;8:248–57. https://doi.org/10.1108/13552540210441166.
[53] Chacón JM, Caminero MA, García-Plaza E, Núñez PJ. Additive manufacturing of PLA structures using fused deposition modelling: effect of process parameters on mechanical properties and their optimal selection. Mater Des 2017;124:143–57. https://doi.org/10.1016/j.matdes.2017.03.065.
[54] Khaliq J, Gurrapu DR, Elfakhri F. Effects of infill line multiplier and patterns on mechanical properties of lightweight and resilient hollow section products manufactured using fused filament fabrication. Polymers (Basel) 2023;15. https://doi.org/10.3390/polym15122585.
[55] Sood AK, Ohdar RK, Mahapatra SS. Parametric appraisal of mechanical property of fused deposition modelling processed parts. Mater Des 2010;31:287–95. https://doi.org/10.1016/j.matdes.2009.06.016.
[56] Ziemian C, Sharma M, Ziemi S. Anisotropic mechanical properties of ABS parts fabricated by fused deposition modelling. Mech Eng 2012. https://doi.org/10.5772/34233.
[57] Tekinalp HL, Kunc V, Velez-Garcia GM, Duty CE, Love LJ, Naskar AK, et al. Highly oriented carbon fiber-polymer composites via additive manufacturing. Compos Sci Technol 2014;105:144–50. https://doi.org/10.1016/j.compscitech.2014.10.009.
[58] Vaezi M, Seitz H, Yang S. A review on 3D micro-additive manufacturing technologies. Int J Adv Manuf Technol 2013;67:1721–54. https://doi.org/10.1007/s00170-012-4605-2.
[59] Boschetto A, Bottini L. Roughness prediction in coupled operations of fused deposition modeling and barrel finishing. J Mater Process Technol 2015;219:181–92. https://doi.org/10.1016/j.jmatprotec.2014.12.021.
[60] He Y, Bi Z, Wang T, Wang L, Lu G, Cui Y, et al. Design and mechanical properties analysis of hexagonal perforated honeycomb metamaterial. Int J Mech Sci 2024;270:109091. https://doi.org/10.1016/j.ijmecsci.2024.109091.
[61] Yanaka W, Nozaki K, Matsumura M, Saleh O, Shin C, Uchida E, et al. Enhancement of internal fit in computer-aided design/manufacturing crowns through optimization of cutting resistance: a quantitative evaluation of feed rate and material properties. J Mech Behav Biomed Mater 2025;170:107093. https://doi.org/10.1016/j.jmbbm.2025.107093.
[62] Kamer MS, Uzay Ç. Investigation of the effect of CNC milling cutting process on the tensile test of PLA samples produced using two different 3D printers with the FDM method. Çukurova Üniversitesi Mühendislik Fakültesi Dergisi 2024;39:599–608. https://doi.org/10.21605/cukurovaumfd.1559927.
[63] Sriya Ambati S, Ambatipudi R. Effect of infill density and infill pattern on the mechanical properties of 3D printed PLA parts. Mater Today Proc 2022;64:804–7. https://doi.org/10.1016/j.matpr.2022.05.312.
[64] Demiral M. Strength in adhesion: a multi-mechanics review covering tensile, shear, fracture, fatigue, creep, and impact behavior of polymer bonding in composites. Polym 2025;17(19):2600. https://doi.org/10.3390/polym17192600.
[65] Kadioglu F, Demiral M. Design of adhesively-bonded single lap joints for automotive applications under compressive loading. Results Eng 2025;25:104176. https://doi.org/10.1016/j.rineng.2025.104176.
[66] Demiral M, Saracyakupoglu T, Şahin B, Köklü U. Minimizing delamination in CFRP laminates: experimental and numerical insights into drilling and punching effects. Polym 2025;17(22):3056. https://doi.org/10.3390/polym17223056.